Available online at www.sciencedirect.com
SCIENCE DIRECT®
PERGAMON
International Journal of Heat and Mass Transfer 46 (2003) 2737–2753
International Journal of HEAT and MASS TRANSFER
www.elsevier.com/locate/ijhmt

Measurement and prediction of pressure drop in two-phase micro-channel heat sinks

Weilin Qu, Issam Mudawar *

Boiling and Two-phase Flow Laboratory, School of Mechanical Engineering, Purdue University, West Lafayette, IN 47907, USA

Received 18 October 2002; received in revised form 13 January 2003

Abstract

This study explores hydrodynamic instability and pressure drop in a water-cooled two-phase micro-channel heat sink containing 21 parallel 231×713 μm micro-channels. Two types of two-phase hydrodynamic instability were identified: severe pressure drop oscillation and mild parallel channel instability. It is shown the severe pressure drop oscillation, which can trigger pre-mature critical heat flux, can be eliminated simply by throttling the flow upstream of the heat sink. Different methods for predicting two-phase pressure drop are assessed for suitability to micro-channel heat-sink design. First, generalized two-phase pressure drop correlations are examined, which include 10 correlations developed for both macro- and mini/micro-channels. A new correlation incorporating the effects of both channel size and coolant mass velocity is proposed which shows better accuracy than prior correlations. The second method consists of a theoretical annular two-phase flow model which, aside from excellent predictive capability, possesses the unique attributes of providing a detailed description of the various transport processes occurring in the micro-channel, as well as fundamental appeal and broader application range than correlations.

Keywords: Micro-channel; Two-phase flow; Boiling; Pressure drop

1. Introduction

The unique attributes of low thermal resistance, compact dimensions, small coolant inventory, low flow rate requirements, and fairly uniform stream-wise temperature render two-phase micro-channel heat sinks a prime contender for thermal management of high-power-density electronic components in many cutting-edge computer, aerospace and medical applications. Implementation of this powerful cooling scheme is hindered by limited understanding of the momentum and thermal transport characteristics of two-phase micro-channels.

Due to the small hydraulic diameter used in two-phase micro-channel heat sinks, 10–1000 μm, excessive pressure drop is always a concern, since these devices are typically used with miniature pumps with limited pumping power capability. Another practical concern is pressure oscillation due to hydrodynamic instabilities. Instabilities must therefore be identified and prevented to ensure safe operation and predictable cooling performance.

A few published studies discuss pressure drop and hydrodynamic instability of flow boiling in mini/micro-channels. Flow boiling pressure drop of refrigerant R-113 in both mini-channel (2.54 mm i.d.) and micro-channel (510 μm i.d.) heat sinks was examined by Bowers and Mudawar [1–3]. They adopted the homogenous equilibrium model to evaluate pressure drop in the two-phase region with good accuracy. Tran et al. [4] studied flow boiling pressure drop of three refrigerants (R-124a, R-12, and R-113) in single tubes (2.46 and 2.92 mm i.d.) and a single rectangular channel (4.06×1.7 mm^2). They evaluated the accelerational component of pressure drop using a separated flow model incorporating Zivi's void fraction correlation [5] and tested five

* Corresponding author. Tel.: +765-494-5705; fax: +765-494-0539.
E-mail address: mudawar@ecn.purdue.edu (I. Mudawar).

0017-9310/03/$ - see front matter
doi:10.1016/S0017-9310(03)00044-9

Nomenclature

A_c	vapor core cross-sectional area
A_{ch}	micro-channel cross-sectional area
A_{p1}, A_{p2}	plenum cross-sectional area
A_t	planform area of heat sink's top surface
Bo	boiling number
C	Martinelli–Chisholm constant
C_{Ef}	liquid droplet concentration in vapor core
c_P	specific heat at constant pressure
D	deposition rate
d_h	hydraulic diameter of micro-channel
$d_{h,c}$	hydraulic diameter of vapor core
f	friction factor
f_{app}	apparent friction factor for developing single-phase liquid flow
f_f	friction factor based on local liquid flow rate
f_{fo}	friction factor based on total flow rate as liquid
Fr	Froude number
G	mass velocity in micro-channel
G_{p1}, G_{p2}	mass velocity in plenums
h	enthalpy
H_{ch}	height of micro-channel
h_{fg}	latent heat of vaporization
j_g	vapor superficial velocity
k	deposition mass transfer coefficient
K_{c1}, K_{c2}	contraction loss coefficient
K_{e1}, K_{e2}	expansion recovery coefficient
L	length of micro-channel
$L^+_{sp,d}$	non-dimensional length of single-phase developing sub-region
$\dot{m}$	mass flow rate per micro-channel
N	number of micro-channels in heat sink
P	pressure
P_c	vapor core perimeter
P_{ch}	micro-channel perimeter
P_W	total electrical power input to heat sink's cartridge heaters
ΔP	pressure drop
ΔP_{c1}, ΔP_{c2}	contraction pressure loss
ΔP_{e1}, ΔP_{e2}	expansion pressure recovery
$\Delta P_{tp,a}$	accelerational component of two-phase pressure drop
$\Delta P_{tp,f}$	frictional component of two-phase pressure drop
q''_{eff}	effective heat flux based on heat sink's top planform area
Re	Reynolds number
Re_f	Reynolds number based on local liquid flow
Re_{fo}	Reynolds number based on total flow as liquid
Re_g	Reynolds number based on local vapor flow
t	time
T	temperature
T_{sat}	saturation temperature
u_c	mean vapor core velocity
u_f	local velocity in liquid film
u_i	interfacial velocity
v	specific volume
v_{fg}	specific volume difference between saturated vapor and saturated liquid
W	width of heat sink
W_{ch}	width of micro-channel
We	Weber number
x_e	thermodynamic equilibrium quality
X_{vt}	Martinelli parameter based on laminar liquid–turbulent vapor flow
X_{vv}	Martinelli parameter based on laminar liquid–laminar vapor flow
y	distance from channel wall
z	axial coordinate

Greek symbols

α	void fraction
β	aspect ratio of micro-channel
β_c	aspect ratio of vapor core
Γ_d	deposition mass transfer rate per unit micro-channel length
Γ_{fg}	evaporation mass transfer rate per unit micro-channel length
δ	liquid film thickness
μ	viscosity
ρ	density
σ	surface tension
τ	shear stress
ϕ^2_f	two-phase frictional multiplier based on local liquid flow rate
ϕ^2_{fo}	two-phase frictional multiplier based on total flow considered as liquid

Subscripts

0	onset of annular flow
a	accelerational
c	vapor core; contraction
e	expansion
Ef	liquid droplet
exp	experimental (measured)
f	liquid; frictional
Ff	liquid film
g	vapor
H	homogeneous
i	interface
in	test module inlet
out	test module outlet
p1, p2	deep, shallow plenum
pred	predicted

sp	single-phase	sp,f	single-phase fully developed sub-region
sp,d	single-phase developing sub-region	tp	two-phase

different macro-channel correlations for the frictional component. Significant deviation between predictions and experimental data led them to develop a new frictional pressure drop correlation that enhanced agreement with the data. Lee and Lee [6] studied flow boiling pressure drop of R-113 in single rectangular channels of 20 mm width and 0.4, 1 and 2 mm height. Zivi's void fraction correlation was also used to determine the accelerational component of pressure drop. Several prior correlations developed for both macro- and mini/micro-channels were tested for frictional component prediction. Most showed large discrepancy except for a modified Lockhart–Martinelli correlation proposed earlier by the same authors [7]. Yu et al. [8] studied flow boiling pressure drop of water in a single tube (2.98 mm i.d.), but did not consider the accelerational pressure drop. They proposed a modified Lockhart–Martinelli correlation to improve their model's predictive capability.

Two-phase hydrodynamic instabilities in parallel mini/micro-channels were addressed by Kandlikar et al. [9] and Hetsroni et al. [10]. Kandlikar et al. studied water flow boiling in a test section containing six parallel 1×1 mm^2 channels. Both inlet and outlet pressures fluctuated with large amplitude, and the magnitude of fluctuation was sometimes so severe that negative pressure drops were measured across the test section. Hetsroni et al. conducted experiments with dielectric liquid Vertel XF in a micro-channel heat sink containing 21 parallel triangular micro-channels having a base dimension of 250 μm. The flow in individual micro-channels alternated between single-phase liquid and elongated vapor bubbles. The amplitude of pressure drop fluctuation increased significantly with increasing heat flux.

The aforementioned studies provide valuable insight into the transport characteristics of two-phase micro-channel heat sinks. However, designers of such devices are faced with a host of unique issues which complicate the implementation of existing knowledge. These include high-aspect-ratio rectangular flow passages, three rather than four-sided heating, parallel channel interactions, and the use of water instead of refrigerants as working fluid. These features have become a standard for devices that are recommended for many high-heat-flux cooling situations, yet virtually no data presently exist which combine all these features.

This study is an investigation into pressure drop and hydrodynamic instability of a water-cooled two-phase micro-channel heat sink. The primary objectives of this study are to (1) provide a new database for the aforementioned micro-channel heat sink geometry, (2) explore different forms of hydrodynamic instability in parallel two-phase micro-channels as well as means of eliminating severe forms of instability, (3) assess the accuracy of previous correlations at predicting pressure drop characteristics, and (4) develop new predictive tools, both empirical and theoretical, for accurate prediction of heat-sink pressure drop.

2. Experimental apparatus and procedure

Fig. 1 shows a schematic of the two-phase coolant-conditioning loop which delivered deionized water to the test module. A constant temperature bath was employed to adjust the test module's inlet temperature, while a condenser situated downstream from the module returned any vapor exiting the module to liquid state. A control valve was situated upstream of the module mainly for flow control, and a second valve downstream to regulate outlet pressure.

Aside from the heat sink itself, the test module consisted of housing, cover plate, and 12 cartridge heaters, as illustrated in Fig. 2. Viewed from above, the heat sink measured 1.0 cm in width and 4.48 cm in length. The micro-channels were formed by cutting 21 of 231-μm wide and 712-μm deep micro-slots into the heat sink's top surface. Four thermocouples were inserted beneath the top surface to measure the heat sink's stream-wise temperature distribution. The underside of the heat sink was bored to accept 12 cartridge heaters. The housing contained deep and shallow plenums both upstream and downstream of the micro-channels to ensure even flow distribution. Two absolute pressure transducers were connected to the deep plenums via pressure taps to measure the inlet and outlet pressures. Also located in the deep plenums were two thermocouples for inlet and outlet temperature measurement. The micro-channels were formed by bolting the cover plate atop the housing. After the test module was assembled, multiple layers of ceramic fiber were wrapped around the heat sink to reduce heat loss to the ambient. An HP data acquisition system interfaced to a PC was employed to record signals from the pressure transducers and thermocouples.

Water in the reservoir was initially deaerated by vigorous boiling for about 1 h to force any dissolved gases to escape to the ambient. The flow loop components were then adjusted to yield the desired operating conditions. After the flow became stable, the heater power input was adjusted to a value below incipient

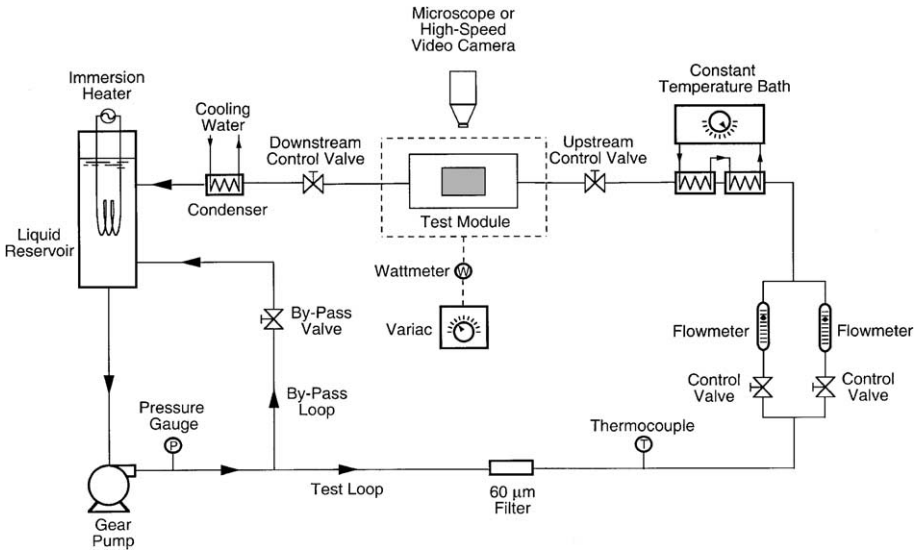

Fig. 1. Schematic of flow loop.

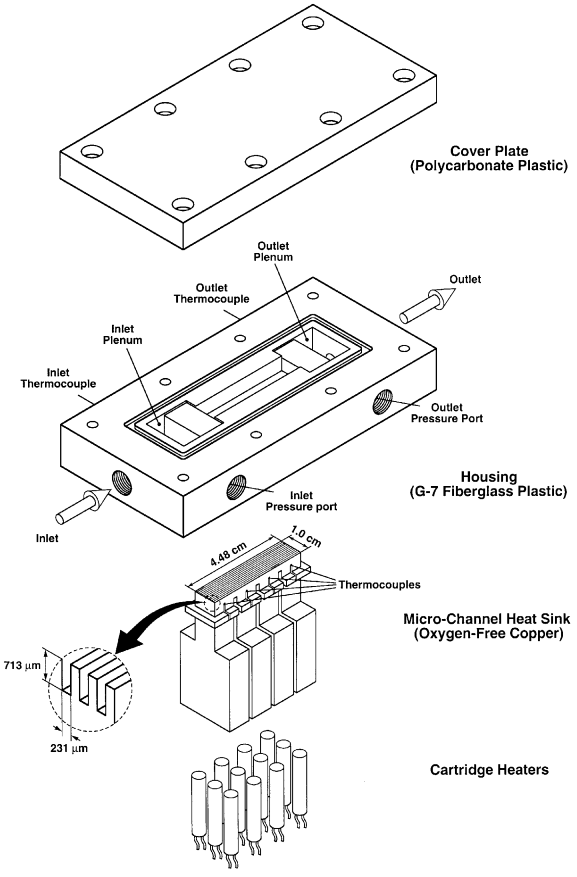

Fig. 2. Test module construction.

boiling. The power was then increased in small increments while the flow loop components were constantly adjusted to restore operating conditions. The heat sink was allowed to reach steady state conditions, when the mean measured pressures and temperatures became constant, after which the pressures and temperatures were recorded at 0.5 s intervals for 5 min. Experimental pressure drop was obtained by subtracting the mean measured outlet pressure from the mean measured inlet pressure, $\Delta P_{\text{exp}} = P_{\text{in}} - P_{\text{out}}$. The test was terminated when the thermodynamic equilibrium quality,

$$x_{\text{e}} = \frac{h - h_{\text{f}}}{h_{\text{fg}}}, \tag{1}$$

reached about 0.2 at the exit.

Heat loss from the test module was estimated to be less than 4%. All heat fluxes presented in this study were therefore based on electrical power input. The accuracy of flow rate and pressure measurements was better than 4% and 3.5%, respectively, and thermocouple error was smaller than ±0.3 °C. Further details of the flow loop, heat-sink design, operating procedure, and heat loss are available in Ref. [11].

The operating conditions for this study were as follows: inlet temperature of $T_{\text{in}} = 30.0$ or 60.0 °C, mass velocity of $G = 134.9$–400.1 kg/m^2 s, and outlet pressure of $P_{\text{out}} = 1.17$ bar. A constant pump exit pressure of 2.0 bar was maintained throughout the study.

3. Hydrodynamic instability

Two types of two-phase hydrodynamic instability were encountered and clearly identified. The first occurred when the upstream control valve was fully open.

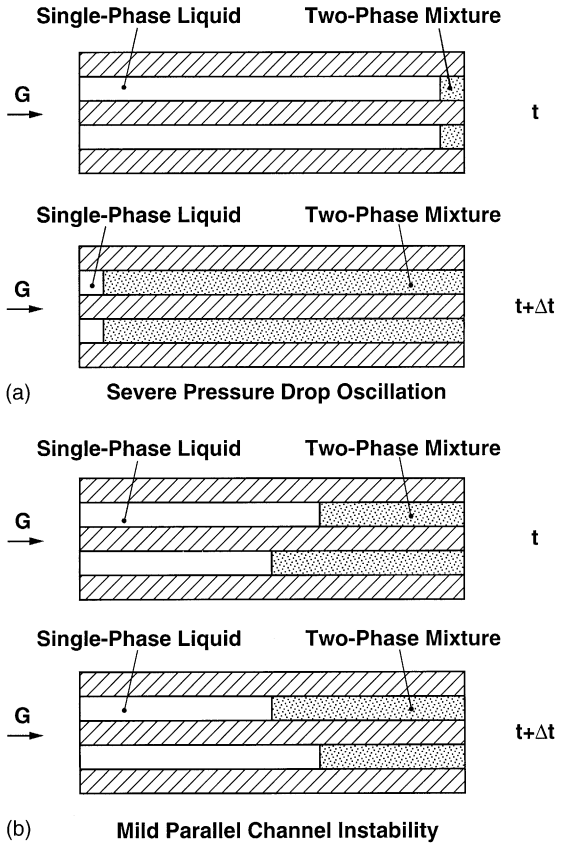

Fig. 3. Top views of two neighboring micro-channels illustrating (a) severe pressure drop oscillation and (b) mild parallel channel instability.

Soon after the heat flux exceeded the incipient boiling value, a significant amount of vapor was produced in the micro-channels, which precipitated a sudden *severe pressure drop oscillation*. A schematic of the observed flow oscillation in two neighboring channels within a short time interval (about 1–5 s) is illustrated in Fig. 3(a). The boiling boundary between the single-phase liquid and two-phase mixture in all 21 channels oscillated back and forth in unison between the inlet and outlet. The oscillation was often so severe that vapor could enter the inlet plenums. This type of instability may be attributed to *interaction between vapor generation in channels and compressible volume in the flow loop upstream of the heat sink*. Vapor generation increases flow resistance in the channels. If the system stiffness is low, such as having a large compressible upstream volume, the increased flow resistance reduces the coolant flow rate, which in turn leads to greater vapor production in the channels. The reduction in flow rate is confined to the heat sink alone since the flow loop is designed to deliver a constant flow rate. Increased flow resistance due to the increase vapor generation now begins to raise the heat sink's upstream pressure. The upstream pressure escalates to a level high enough to push the vapor completely out from the channels. If certain conditions are met, a periodic behavior may become self-sustained, which is classified as pressure drop oscillation [12,13]. This type of hydrodynamic instability is highly undesirable as it induces not only severe flow oscillation, but also pre-mature critical heat flux (CHF). CHF can occur at unusually low heat fluxes when the liquid feedback is delayed and the channels are occupied mostly by the vapor phase for an extended period of time.

The severe pressure drop oscillation was virtually eliminated by throttling the flow immediately upstream of the test module. During the tests, the upstream control valve was throttled until the pump exit pressure reached 2.0 bar, about 0.5 bar higher than for a fully open valve. With this added system stiffness, the boiling boundary was observed to fluctuate at low heat fluxes between micro-channels in a random manner as illustrated in Fig. 3(b). The spatial amplitude of fluctuation of the boiling boundary was reduced significantly in all micro-channels compared to tests with the severe pressure drop oscillation. The flow pattern within each channel oscillated between bubble nucleation and slug flow. At medium to high heat fluxes, the boiling boundaries propagated upstream, and the flow oscillated between slug and annular in the channel upstream and was predominantly annular downstream. This type of instability can be classified as *mild parallel channel instability, intrinsic to the test module itself*. It is essentially the result of density wave oscillation within each channel and feedback interaction between channels [13].

Hydrodynamic instabilities affect both inlet and outlet pressures, and can introduce appreciable uncertainty in pressure drop measurement. Fig. 4(a) and (b) show temporal records of inlet and outlet pressures when the heat sink was undergoing the severe pressure drop oscillation and mild parallel channel instability, respectively. The operating conditions for the two situations are the same except for power input and the upstream throttling for the parallel channel instability. Even though a much lower heat flux was applied in the pressure drop oscillation case (Fig. 4(a)) to avoid premature CHF, the pressure fluctuations are far more severe. Furthermore, the pressure fluctuations appear to form with fairly constant frequency. Fluctuations in the parallel channel instability case (Fig. 4(b)) are both small and random.

All pressure drop data reported in the following sections were therefore obtained with the upstream control valve throttled. The data were all subject to the mild parallel channel instability, but free from the severe pressure drop oscillation. Future researchers are urged to adopt this effective throttling technique in all two-phase heat sink studies.

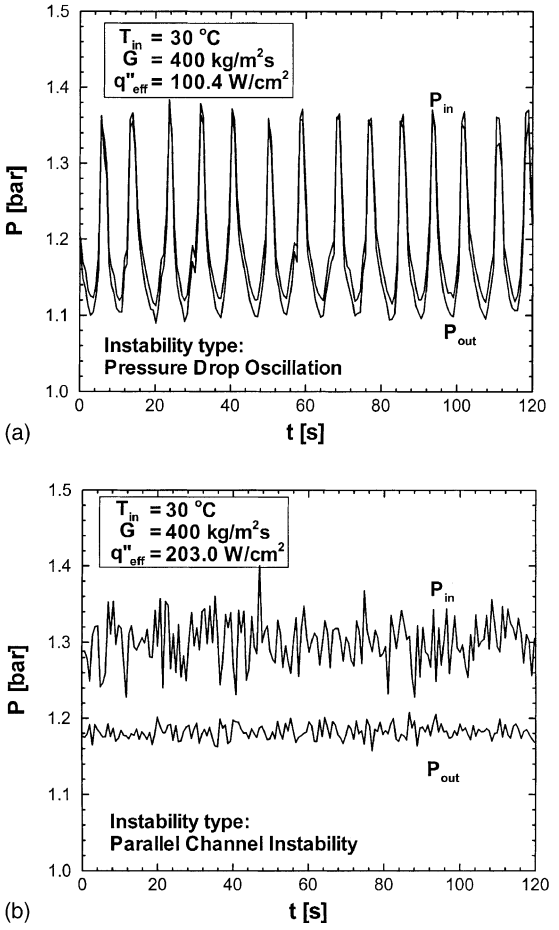

Fig. 4. Temporal records of inlet and outlet pressures during (a) pressure drop oscillation and (b) parallel channel instability.

4. Pressure drop determination

Since the pressure transducers were connected to the deep plenums of the heat sink's housing, the measured pressure drop is the sum of pressure drops across the inlet plenums, micro-channels, outlet plenums, as well as pressure losses and recoveries associated with the contractions and expansions, respectively, between consecutive regions. Pressure calculations reveal the pressure drop associated with the inlet and outlet plenums is miniscule by comparison with the pressure drop in the micro-channels themselves.

As indicated before, water was supplied into the heat sink in sub-cooled state ($T_{in} < T_{sat}$). It is assumed that the water maintains a single-phase liquid state until it reaches zero thermodynamic equilibrium quality, $x_e = 0$. The flow is then gradually converted to a saturated two-phase mixture immediately downstream from the location of zero quality. As illustrated in Fig. 5, each micro-channel is divided into a single-phase region,

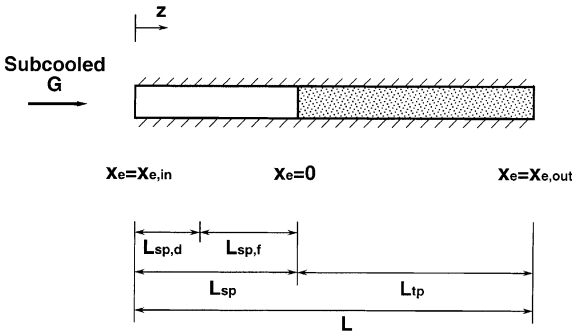

Fig. 5. Schematic of flow regions in a micro-channel.

$$L_{sp} = \frac{N\dot{m}c_{P,f}(T_{sat} - T_{in})}{q''_{eff}W}, \tag{2}$$

and a two-phase region, $L_{tp} = L - L_{sp}$. T_{sat} in Eq. (2) is the saturation temperature at the location of $x_e = 0$, which is evaluated using the measured mean inlet pressure, P_{in}, since pressure drop across the single-phase region is quite small. q''_{eff} in Eq. (2) denotes the effective input heat flux based on the heat sink's top planform area, $q''_{eff} = P_W/A_t$, where $A_t = 1.0 \times 4.48$ cm^2.

The single-phase region is further divided into developing and fully developed sub-regions. For the present tests, the highest Reynolds number based on channel inlet liquid conditions is about 303, which is well within the laminar range. The following equations are employed to evaluate the length of the two single-phase sub-regions [14].

$$L_{sp,d} = 0.0785 Re_{in} d_h, \tag{3}$$

and

$$L_{sp,f} = L_{sp} - L_{sp,d}. \tag{4}$$

Neglecting the pressure drop in the plenums, the total heat sink pressure drop can be expressed as

$$\Delta P_{pred} = \Delta P_{c1} + \Delta P_{c2} + \Delta P_{sp,d} + \Delta P_{sp,f} + \Delta P_{tp} + \Delta P_{e2} + \Delta P_{e1}, \tag{5}$$

where ΔP_{c1} and ΔP_{c2} are the inlet contraction pressure losses, ΔP_{e2} and ΔP_{e1} are the outlet expansion pressure recoveries, $\Delta P_{sp,d}$ and $\Delta P_{sp,f}$ denote pressure drops in the single-phase developing and fully developed sub-regions, and ΔP_{tp} is the pressure drop in the two-phase region. All components of ΔP_{pred} in Eq. (5) except ΔP_{tp} are fairly straightforward and given in Table 1 [14–16]. ΔP_{tp} is determined using two distinct predictive methods: (1) generalized two-phase pressure drop correlations and (2) a new annular two-phase flow model.

The pressure drop in the micro-channel two-phase region can be expressed as the sum of accelerational and frictional components.

Table 1
Micro-channel heat sink pressure-drop components

Component	
$\Delta P_{c1}, \Delta P_{c2}$	$\Delta P_{c1} = \frac{v_f}{2}(G_{p2,in}^2 - G_{p1,in}^2) + \frac{K_{c1} v_f}{2} G_{p2,in}^2$
	$\Delta P_{c2} = \frac{v_f}{2}(G^2 - G_{p2,in}^2) + \frac{K_{c2} v_f}{2} G^2$
	K_{c1} and K_{c2} from Table 6.2 in Ref. [15]
$\Delta P_{e1}, \Delta P_{e2}$	$\Delta P_{e2} = \frac{v_f + x_{e,out} v_{fg}}{2}(G_{p2,out}^2 - G^2) + \frac{K_{e2}(v_f + x_{e,out} v_{fg})}{2} G^2; \quad K_{e1} = \left(1 - \frac{NA_{ch}}{A_{p2}}\right)^2$
	$\Delta P_{e1} = \frac{v_f + x_{e,out} v_{fg}}{2}(G_{p1,out}^2 - G_{p2,out}^2) + \frac{K_{e1}(v_f + x_{e,out} v_{fg})}{2} G_{p2,out}^2; \quad K_{e1} = \left(1 - \frac{A_{p2}}{A_{p1}}\right)^2$
$\Delta P_{sp,f}$	$\Delta P_{sp,f} = \frac{2 f_{sp,f} G^2 L_{sp,f} v_f}{d_h}$
	$f_{sp,f} Re_{sp,f} = 24(1 - 1.355\beta + 1.947\beta^2 - 1.701\beta^3 + 0.956\beta^4 - 0.254\beta^5); \quad Re_{sp,f} = \frac{G d_h}{\mu_{sp,f}}; \quad \beta = \frac{W_{ch}}{H_{ch}}$
$\Delta P_{sp,d}$	$\Delta P_{sp,d} = \frac{2 f_{app} G^2 L_{sp,d} v_f}{d_h}$
	$f_{app} = \frac{1}{Re_{sp,d}}\left[3.44(L_{sp,d}^+)^{-0.5} + \frac{1.089/(4L_{sp,d}^+) + f_{sp,d} Re_{sp,d} - 3.44(L_{sp,d}^+)^{-0.5}}{1 + 1.31 \times 10^{-4}(L_{sp,d}^+)^{-2}}\right]; \quad L_{sp,d}^+ = \frac{L_{sp,d}}{Re_{sp,d} d_h}$
	$f_{sp,d} Re_{sp,d} = 24(1 - 1.355\beta + 1.947\beta^2 - 1.701\beta^3 + 0.956\beta^4 - 0.254\beta^5); \quad Re_{sp,d} = \frac{G d_h}{\mu_{sp,d}}$

$$\Delta P_{tp} = \Delta P_{tp,a} + \Delta P_{tp,f}. \tag{6}$$

A large number of correlations developed under the framework of the homogeneous equilibrium flow model and the separated flow model are used to evaluate both components [16]. In the present study, six popular macro-channel correlations and four correlations developed specifically for mini/micro-channels are examined, which are summarized in Table 2.

Among the six macro-channel methods (1–6), the first is based on the homogeneous equilibrium flow model, while the other five employ the separated flow model and the Martinelli void fraction correlation to evaluate $\Delta P_{tp,a}$ [16]. Fig. 6 compares the variations of ΔP_{exp} and ΔP_{pred} with q''_{eff} for $G = 255$ kg/m^{2}s. and $T_{in} = 60$ °C. While most correlations overpredict pressure drop by large margins, better agreement is achieved with the Lockhart–Martinelli correlation based on laminar liquid and laminar vapor flow (correlation 2). The predictive capability of the macro-channel correlations is further illustrated in Fig. 7(a)–(f) for all operating conditions of the present study. The mean absolute error (MAE) of each correlation,

$$\mathrm{MAE} = \frac{1}{M}\sum \frac{|\Delta P_{pred} - \Delta P_{exp}|}{\Delta P_{exp}} \times 100\% \tag{7}$$

is provided in both Table 2 and Fig. 7(a)–(f).

Interestingly, the homogeneous flow model provides better predictions than three of the macro-channel separated flow correlations. Nonetheless, the homogeneous flow model shows significant departure from the present data. The same model showed satisfactory pressure drop predictions of Bowers and Mudawar's micro-channel flow boiling tests with R-113 [1–3]. This may be explained by fundamental differences in flow boiling behavior in micro-channels between water and R-113. The latter refrigerant features low surface tension and small contact angle, which results in bubble departure diameters one or two orders of magnitude smaller than those for water. Those differences were recently demonstrated experimentally by Mukherjee and Mudawar [22] by comparing results for water and FC-72, the latter being a fluorochemical with thermophysical properties fairly similar to those of R-113.

The Martinelli–Nelson correlation (4), Chisholm correlation (5), and Friedel correlation (6), which are all very popular macro-channel correlations, show the greatest MAE and are deemed unsuitable for micro-channel pressure drop calculations. A possible reason for their large MAE is that they were developed for turbulent flow, which is prevalent in macro-channels, while the low coolant flow rate and small channel size of micro-channels yield mostly laminar flow for the liquid phase and laminar or turbulent flow for the vapor phase. For example, Re_f and Re_g in the present tests are consistently less than 2000, which correspond to laminar liquid and laminar vapor flow. This also explains why correlation 2 produces better agreement with experimental data than the other five.

Table 2
Generalized two-phase pressure-drop correlations

Correlation (or model)	Reference	Frictional component, $\Delta P_{tp,f}$	Accelerational component, $\Delta P_{tp,a}$	MAE (%)
1	Homogeneous model [16]	$\Delta P_{tp,f} = \frac{2f_{tp}G^2L_{tp}v_f}{d_h}\left[1+\frac{x_{e,out}}{2}\left(\frac{v_{fg}}{v_f}\right)\right]; \quad f_{tp}=0.003$	$\Delta P_{tp,a} = G^2 v_f x_{e,out}$	89.2
2	Lockhart–Martinelli (laminar liquid–laminar vapor) [17,18]	$\Delta P_{tp,f} = \frac{L_{tp}}{x_{e,out}}\int_0^{x_{e,out}} \frac{2f_f G^2(1-x_e)^2 v_f}{d_h}\phi_f^2\,dx_e$ $f_f Re_f = 24(1-1.355\beta+1.947\beta^2-1.701\beta^3+0.956\beta^4-0.254\beta^5);$ $Re_f = \frac{G(1-x_e)d_h}{\mu_f}$ $\phi_f^2 = 1+\frac{C}{X_{vv}}+\frac{1}{X_{vv}^2}, \quad C=5;$ $X_{vv} = \left(\frac{\mu_f}{\mu_g}\right)^{0.5}\left(\frac{1-x_e}{x_e}\right)^{0.5}\left(\frac{v_f}{v_g}\right)^{0.5}$	$\Delta P_{tp,a} = G^2 v_f\left[\frac{x_{e,out}^2}{\alpha_{out}}\left(\frac{v_g}{v_f}\right)+\frac{(1-x_{e,out})^2}{1-\alpha_{out}}-1\right]$ $\alpha_{out} = 1-\frac{1}{\sqrt{1+\frac{20}{X_{vv,out}}+\frac{1}{X_{vv,out}^2}}}$	28.6
3	Lockhart Martinelli (laminar liquid–turbulent vapor) [17,18]	$\Delta P_{tp,f} = \frac{L_{tp}}{x_{e,out}}\int_0^{x_{e,out}} \frac{2f_f G^2(1-x_e)^2 v_f}{d_h}\phi_f^2\,dx_e$ $\phi_f^2 = 1+\frac{C}{X_{vt}}+\frac{1}{X_{vt}^2}; \quad C=12;$ $X_{vt} = \left(\frac{f_f Re_g^{0.25}}{0.079}\right)^{0.5}\left(\frac{1-x_e}{x_e}\right)\left(\frac{v_f}{v_g}\right)^{0.5}; \quad Re_g = \frac{Gx_e d_h}{\mu_g}$	$\Delta P_{tp,a} = G^2 v_f\left[\frac{x_{e,out}^2}{\alpha_{out}}\left(\frac{v_g}{v_f}\right)+\frac{(1-x_{e,out})^2}{1-\alpha_{out}}-1\right]$ $\alpha_{out} = 1-\frac{1}{\sqrt{1+\frac{20}{X_{vt,out}}+\frac{1}{X_{vt,out}^2}}}$	44.6
4	Martinelli–Nelson [19]	$\Delta P_{tp,f} = \frac{2f_{fo}G^2L_{tp}v_f}{d_h}r_1(x_{e,out},P); \quad r_1(x_{e,out},P)$ from Fig. 4 in Ref. [19] $f_{fo}Re_{fo} = 24(1-1.355\beta+1.947\beta^2-1.701\beta^3+0.956\beta^4-0.254\beta^5);$ $Re_{fo} = \frac{Gd_h}{\mu_f}$	$\Delta P_{tp,a} = G^2 v_f r_2(x_{e,out},P);\ r_2(x_{e,out},P)$ from Fig. 6 in Ref. [19]	165.5
5	Chisholm [20]	$\Delta P_{tp,f} = \frac{2f_{fo}G^2v_f}{d_h}\frac{L_{tp}}{x_{e,out}}\int_0^{x_{e,out}}\phi_{fo}^2\,dx_e$ $\phi_{fo}^2 = 1+(\Gamma^2-1)[Bx_e^{0.5}(1-x_e)^{0.5}+x_e];$ $\Gamma = \left(\frac{v_g}{v_f}\right)^{0.5}\left(\frac{\mu_g}{\mu_f}\right)^{0.5}; \quad B$ from Table 2 in Ref. [20]	$\Delta P_{tp,a} = G^2 v_f\left[\frac{x_{e,out}^2}{\alpha_{out}}\left(\frac{v_g}{v_f}\right)+\frac{(1-x_{e,out})^2}{1-\alpha_{out}}-1\right]$ $\alpha_{out} = 1-\frac{1}{\sqrt{1+\frac{20}{X_{vv,out}}+\frac{1}{X_{vv,out}^2}}}$	378.4

6	Friedel [16]	$\Delta P_{\mathrm{tp,f}} = \dfrac{2f_{\mathrm{fo}}G^2v_{\mathrm{f}}}{d_{\mathrm{h}}}\dfrac{L_{\mathrm{tp}}}{x_{\mathrm{e,out}}}\displaystyle\int_0^{x_{\mathrm{e,out}}}\phi_{\mathrm{fo}}^2\,\mathrm{d}x_{\mathrm{e}}$ $\phi_{\mathrm{fo}}^2 = A_1 + \dfrac{3.34A_2A_3}{Fr_{\mathrm{H}}^{0.045}We_{\mathrm{H}}^{0.035}};$ $A_1 = (1-x_{\mathrm{e}})^2 + x_{\mathrm{e}}^2\left(\dfrac{v_{\mathrm{g}}}{v_{\mathrm{f}}}\right)\left(\dfrac{\mu_{\mathrm{g}}}{\mu_{\mathrm{f}}}\right);\quad A_2 = x_{\mathrm{e}}^{0.78}(1-x_{\mathrm{e}})^{0.224}$ $A_3 = \left(\dfrac{v_{\mathrm{g}}}{v_{\mathrm{f}}}\right)^{0.91}\left(\dfrac{\mu_{\mathrm{g}}}{\mu_{\mathrm{f}}}\right)^{0.19}\left(1-\dfrac{\mu_{\mathrm{g}}}{\mu_{\mathrm{f}}}\right)^{0.7};$ $Fr_{\mathrm{H}} = \dfrac{G^2}{gd_{\mathrm{h}}\rho_{\mathrm{H}}^2};\quad We_{\mathrm{H}} = \dfrac{G^2d_{\mathrm{h}}}{\rho_{\mathrm{H}}\sigma};\quad \rho_{\mathrm{H}} = \dfrac{1}{x_{\mathrm{e}}v_{\mathrm{g}} + (1-x_{\mathrm{e}})v_{\mathrm{f}}}$	$\Delta P_{\mathrm{tp,a}} = G^2v_{\mathrm{f}}\left[\dfrac{x_{\mathrm{e,out}}^2}{\alpha_{\mathrm{out}}}\left(\dfrac{v_{\mathrm{g}}}{v_{\mathrm{f}}}\right) + \dfrac{(1-x_{\mathrm{e,out}})^2}{1-\alpha_{\mathrm{out}}} - 1\right]$ $\alpha_{\mathrm{out}} = 1 - \dfrac{1}{\sqrt{1 + \frac{20}{X_{\mathrm{vv,out}}} + \frac{1}{X_{\mathrm{vv,out}}^2}}}$	355.0
7	Mishima and Hibiki [21]	$\Delta P_{\mathrm{tp,f}} = \dfrac{L_{\mathrm{tp}}}{x_{\mathrm{e,out}}}\displaystyle\int_0^{x_{\mathrm{e,out}}}\dfrac{2f_{\mathrm{f}}G^2(1-x_{\mathrm{e}})^2v_{\mathrm{f}}}{d_{\mathrm{h}}}\phi_{\mathrm{f}}^2\,\mathrm{d}x_{\mathrm{e}}$ $\phi_{\mathrm{f}}^2 = 1 + \dfrac{C}{X_{\mathrm{vv}}} + \dfrac{1}{X_{\mathrm{vv}}^2};\quad C = 21[1-\exp(-0.319\times10^3d_{\mathrm{h}})];$ $X_{\mathrm{vv}} = \left(\dfrac{\mu_{\mathrm{f}}}{\mu_{\mathrm{g}}}\right)^{0.5}\left(\dfrac{1-x_{\mathrm{e}}}{x_{\mathrm{e}}}\right)^{0.5}\left(\dfrac{v_{\mathrm{f}}}{v_{\mathrm{g}}}\right)^{0.5}$	$\Delta P_{\mathrm{tp,a}} = G^2v_{\mathrm{f}}\left[\dfrac{x_{\mathrm{e,out}}^2}{\alpha_{\mathrm{out}}}\left(\dfrac{v_{\mathrm{g}}}{v_{\mathrm{f}}}\right) + \dfrac{(1-x_{\mathrm{e,out}})^2}{1-\alpha_{\mathrm{out}}} - 1\right]$ $\alpha_{\mathrm{out}} = \dfrac{1}{1 + \left(\frac{1-x_{\mathrm{e,out}}}{x_{\mathrm{e,out}}}\right)\left(\frac{v_{\mathrm{f}}}{v_{\mathrm{g}}}\right)^{2/3}}$	13.9
8	Tran et al. [4]	$\Delta P_{\mathrm{tp,f}} = \dfrac{2f_{\mathrm{fo}}G^2v_{\mathrm{f}}}{d_{\mathrm{h}}}\dfrac{L_{\mathrm{tp}}}{x_{\mathrm{e,out}}}\displaystyle\int_0^{x_{\mathrm{e,out}}}\phi_{\mathrm{fo}}^2\,\mathrm{d}x_{\mathrm{e}}$ $\phi_{\mathrm{fo}}^2 = 1 + (4.3\Gamma^2 - 1)[N_{\mathrm{conf}}x_{\mathrm{e}}^{0.875}(1-x_{\mathrm{e}})^{0.875} + x_{\mathrm{e}}^{1.75}]$ $\Gamma = \left(\dfrac{v_{\mathrm{g}}}{v_{\mathrm{f}}}\right)^{0.5}\left(\dfrac{\mu_{\mathrm{g}}}{\mu_{\mathrm{f}}}\right)^{0.5};\quad N_{\mathrm{conf}} = \left[\dfrac{\sigma}{g(\rho_{\mathrm{f}}-\rho_{\mathrm{g}})}\right]^{0.5}/d_{\mathrm{h}}$	$\Delta P_{\mathrm{tp,a}} = G^2v_{\mathrm{f}}\left[\dfrac{x_{\mathrm{e,out}}^2}{\alpha_{\mathrm{out}}}\left(\dfrac{v_{\mathrm{g}}}{v_{\mathrm{f}}}\right) + \dfrac{(1-x_{\mathrm{e,out}})^2}{1-\alpha_{\mathrm{out}}} - 1\right]$ $\alpha_{\mathrm{out}} = \dfrac{1}{1 + \left(\frac{1-x_{\mathrm{e,out}}}{x_{\mathrm{e,out}}}\right)\left(\frac{v_{\mathrm{f}}}{v_{\mathrm{g}}}\right)^{2/3}}$	828.3
9	Lee and Lee [6]	$\Delta P_{\mathrm{tp,f}} = \dfrac{L_{\mathrm{tp}}}{x_{\mathrm{e,out}}}\displaystyle\int_0^{x_{\mathrm{e,out}}}\dfrac{2f_{\mathrm{f}}G^2(1-x_{\mathrm{e}})^2v_{\mathrm{f}}}{d_{\mathrm{h}}}\phi_{\mathrm{f}}^2\,\mathrm{d}x_{\mathrm{e}}$ $\phi_{\mathrm{f}}^2 = 1 + \dfrac{C}{X_{\mathrm{vt}}} + \dfrac{1}{X_{\mathrm{vt}}^2};\quad C = 6.185\times10^{-2}Re_{\mathrm{fo}}^{0.726};$ $X_{\mathrm{vt}} = \left(\dfrac{f_{\mathrm{f}}Re_{\mathrm{g}}^{0.25}}{0.079}\right)^{0.5}\left(\dfrac{1-x_{\mathrm{e}}}{x_{\mathrm{e}}}\right)\left(\dfrac{v_{\mathrm{f}}}{v_{\mathrm{g}}}\right)^{0.5}$	$\Delta P_{\mathrm{tp,a}} = G^2v_{\mathrm{f}}\left[\dfrac{x_{\mathrm{e,out}}^2}{\alpha_{\mathrm{out}}}\left(\dfrac{v_{\mathrm{g}}}{v_{\mathrm{f}}}\right) + \dfrac{(1-x_{\mathrm{e,out}})^2}{1-\alpha_{\mathrm{out}}} - 1\right]$ $\alpha_{\mathrm{out}} = \dfrac{1}{1 + \left(\frac{1-x_{\mathrm{e,out}}}{x_{\mathrm{e,out}}}\right)\left(\frac{v_{\mathrm{f}}}{v_{\mathrm{g}}}\right)^{2/3}}$	19.1

(*continued on next page*)

Table 2 (*continued*)

Correlation (or model)	Reference	Frictional component, $\Delta P_{tp,f}$	Accelerational component, $\Delta P_{tp,a}$	MAE (%)
10	Yu et al. [8]	$\Delta P_{tp,f} = \frac{L_{tp}}{x_{e,out}} \int_0^{x_{e,out}} \frac{2f_f G^2 (1-x_e)^2 v_f}{d_h} \phi_f^2 \, dx_e$ $\phi_f^2 = \frac{1}{X_{vt}^{1.9}}; \quad X_{vt} = \left(\frac{f_f Re_g^{0.2}}{0.046}\right)^{0.5} \left(\frac{1-x_e}{x_e}\right) \left(\frac{v_f}{v_g}\right)^{0.5}$	$\Delta P_{tp,a} = G^2 v_f \left[\frac{x_{e,out}^2}{\alpha_{out}} \left(\frac{v_g}{v_f}\right) + \frac{(1-x_{e,out})^2}{1-\alpha_{out}} - 1\right]$ $\alpha_{out} = \frac{1}{1 + \left(\frac{1-x_{e,out}}{x_{e,out}}\right) \left(\frac{v_f}{v_g}\right)^{2/3}}$	48.0
11	Qu and Mudawar (present study)	$\Delta P_{tp,f} = \frac{L_{tp}}{x_{e,out}} \int_0^{x_{e,out}} \frac{2f_f G^2 (1-x_e)^2 v_f}{d_h} \phi_f^2 \, dx_e$ $\phi_f^2 = 1 + \frac{C}{X_{vv}} + \frac{1}{X_{vv}^2}$ $C = 21[1 - \exp(-0.319 \times 10^3 d_h)](0.00418G + 0.0613);$ $X_{vv} = \left(\frac{\mu_f}{\mu_g}\right)^{0.5} \left(\frac{1-x_e}{x_e}\right)^{0.5} \left(\frac{v_f}{v_g}\right)^{0.5}$	$\Delta P_{tp,a} = G^2 v_f \left[\frac{x_{e,out}^2}{\alpha_{out}} \left(\frac{v_g}{v_f}\right) + \frac{(1-x_{e,out})^2}{1-\alpha_{out}} - 1\right]$ $\alpha_{out} = \frac{1}{1 + \left(\frac{1-x_{e,out}}{x_{e,out}}\right) \left(\frac{v_f}{v_g}\right)^{2/3}}$	12.4

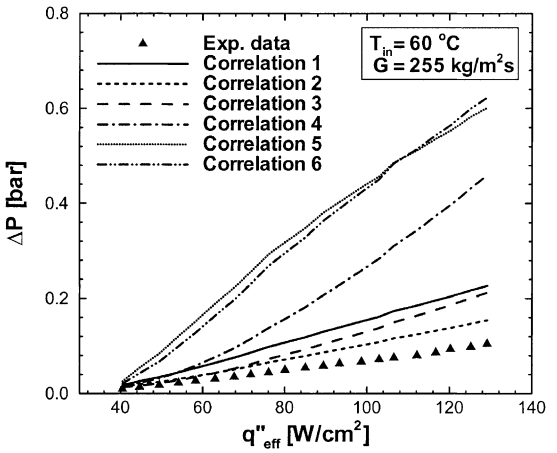

Fig. 6. Comparison of pressure drop data with macro-channel correlation predictions for $T_{in} = 60$ °C and $G = 255$ kg/m^{2}s.

The four remaining correlations in Table 2 (7–10) were developed from mini/micro-channel pressure drop data, and are all based on the separated flow model and employ the Zivi void fraction correlation [5] to evaluate $\Delta P_{tp,a}$. Figs. 8 and 9(a)–(d), compare ΔP_{pred} to ΔP_{exp} for these correlations. The Tran et al. correlation (8) is excluded from Fig. 8 because it predicts unusually small values compared to the data.

The Mishima and Hibiki's correlation (7) is based on the combination of laminar liquid and laminar vapor flow, and accounts for channel size effect by incorporating channel hydraulic diameter in the Martinelli–Chisholm constant C [21]. With a MAE of 13.9%, this correlation yields the most accurate predictions of all previous correlations. The Tran et al. correlation (8), on the other hand, adopts the turbulent liquid and turbulent vapor flow combination [4], which may explain its unusually large MAE. Both the Lee and Lee correlation (9) and Yu et al. correlation (10) utilize the combination of laminar liquid and turbulent vapor flow. In the Lee and Lee correlation, the liquid Reynolds number is incorporated into the Martinelli–Chisholm constant C to reflect the effects of both channel size and coolant flow rate [6]. The Lee and Lee correlation provides reasonably accurate predictions with a MAE of 19.1%. The Yu et al. correlation underpredicts the experimental data by a relatively large margin.

In an effort to improve predictive accuracy, the authors of the present study modified the Mishima and Hibiki correlation by incorporating a mass velocity term. This new correlation is listed as correlation 11 in Table 2. Fig. 10(a) and (b) show the effectiveness of the new correlation at predicting the pressure drop data. While its MAE is only slightly better than the Mishima and Hibiki correlation (12.4% versus 13.9%), the new

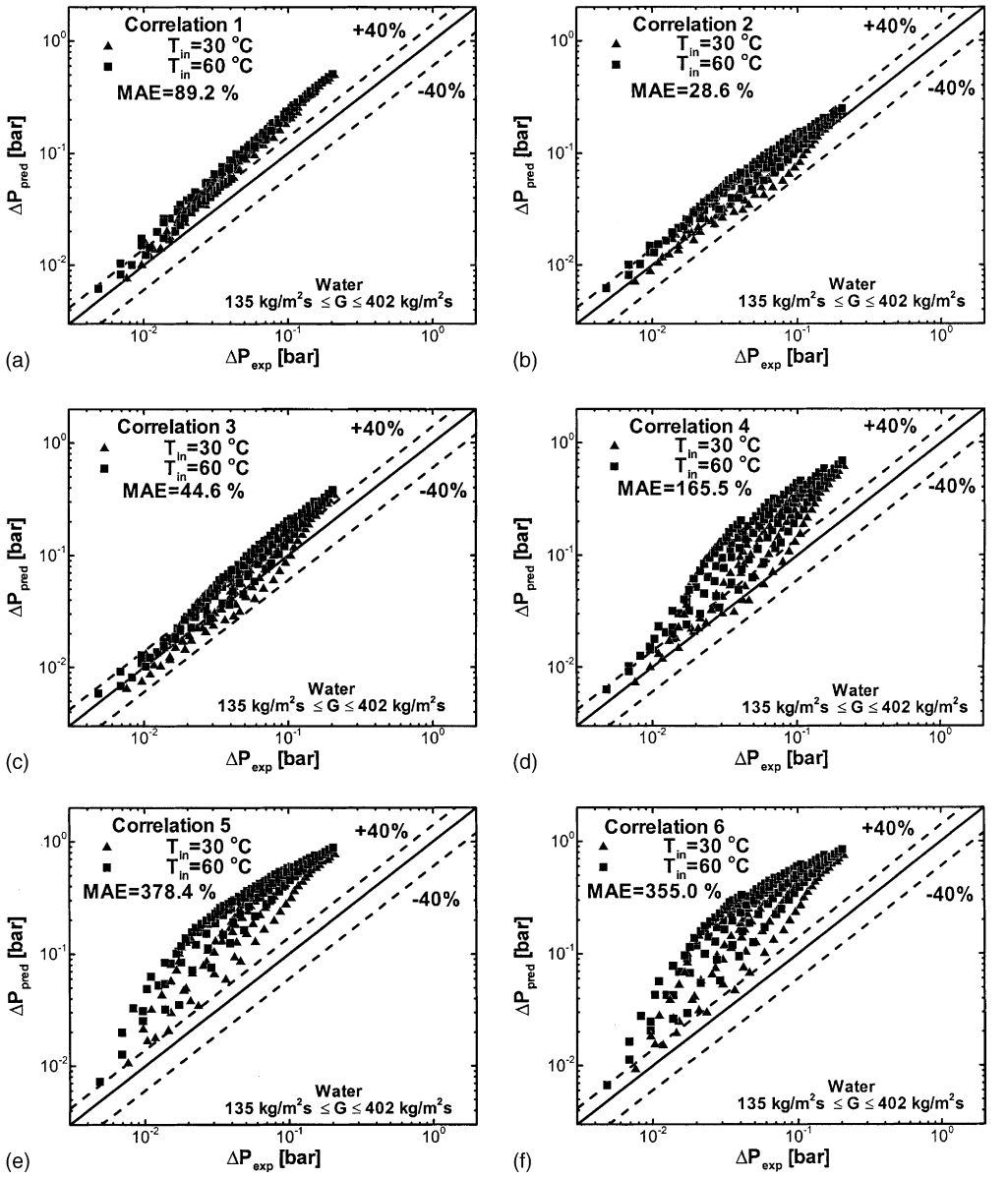

Fig. 7. Comparison of pressure drop data with predictions of (a) homogeneous equilibrium flow model [16], and macro-channel correlations of (b) Lockhart–Martinelli (laminar liquid–laminar vapor) [17,18], (c) Lockhart–Martinelli (laminar liquid–turbulent vapor) [17,18], (d) Martinelli–Nelson [19], (e) Chisholm [20], and (f) Friedel [16].

correlation is recommended because it accounts for the effects of both channel size and coolant mass velocity.

5. Annular two-phase flow model

In a previous paper by the present authors [11], an annular two-phase flow model was developed, which is specifically tailored to water-cooled micro-channel heat sinks. The model incorporates the unique features of micro-channel flow boiling and is capable of accurately predicting the saturated boiling heat transfer coefficient. In the present paper, the annular two-phase flow model is used to evaluate ΔP_{tp}.

The physical basis for the model lies in identification of annular flow as the dominant pattern at moderate to high heat fluxes. Fig. 11(a) illustrates the hydrodynamic characteristics of the annular flow in a micro-channel. The vapor phase flows along the channel center as a continuous vapor core. A portion of the liquid phase

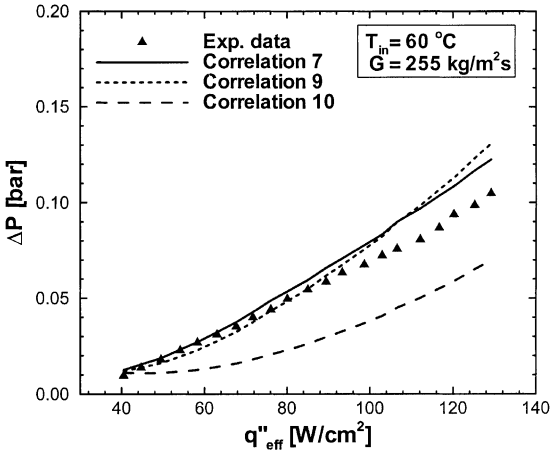

Fig. 8. Comparison of pressure drop data with mini/micro-channel correlation predictions for $T_{in} = 60$ °C and $G = 255$ kg/m^{2}s.

flows as a thin film along the channel wall, while the other portion is entrained in the vapor core as liquid droplets. A simplified representation of the annular flow pattern is given in Fig. 11(b). The thickness of the annular liquid film is assumed to be uniform along the channel circumference, and small compared to the hydraulic diameter. The interface between liquid film and vapor core is fairly smooth due to strong surface tension effects in micro-channels. Mass is exchanged between the liquid film and vapor core by interfacial evaporation and droplet deposition. Evaporation occurs only at the interface, since the entrained droplets have a short residence time in a micro-channel and are remote from the heated wall. Entrainment of liquid droplets into the vapor core is assumed to take place entirely at the onset of annular flow regime development. Γ_{fg} and Γ_{d} in Fig. 11(b) denote, respectively, the evaporation and deposition mass transfer rates per unit channel length.

The primary parameters of annular flow model are the liquid film mass flow rate, $\dot{m}_{Ff}$, liquid film thickness, δ, pressure gradient, $-(dP/dz)$, and interfacial shear stress, τ_i. Equations relating these parameters are established by applying fundamental conservation equations to both the liquid film and vapor core and summarized in Table 3. A brief overview on the model development is given below; further details are left to Ref. [11] for brevity.

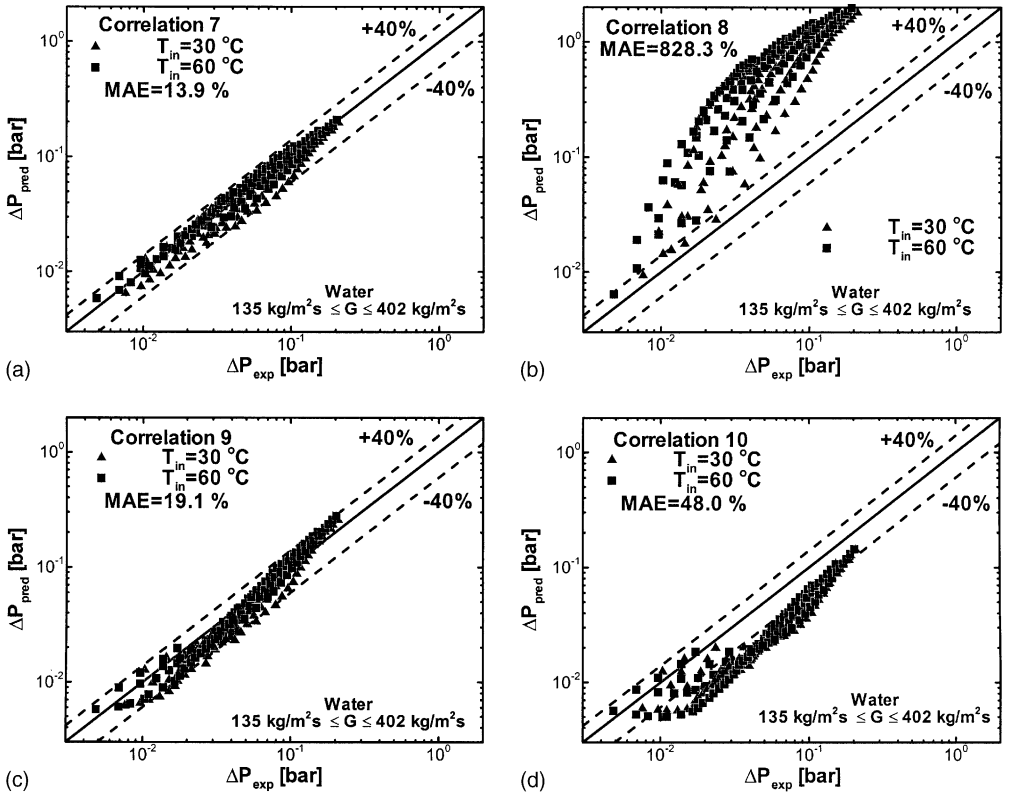

Fig. 9. Comparison of pressure drop data with predictions of mini/micro-channel correlations of (a) Mishima and Hibiki [21], (b) Tran et al. [4], (c) Lee and Lee [6], and (d) Yu et al. [8].

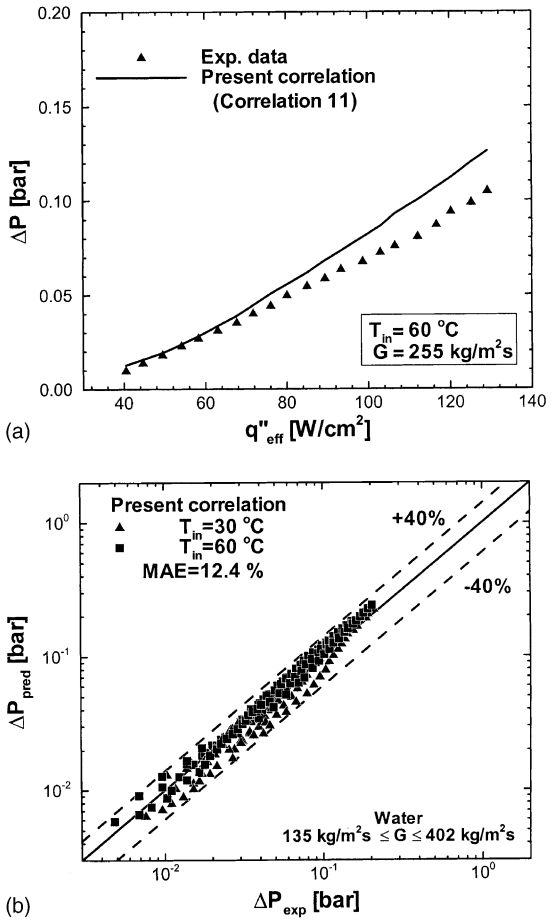

Fig. 10. Comparison of present correlation predictions with pressure drop data for (a) $T_{in} = 60$ °C and $G = 255$ kg/m^{2}s, and (b) entire database.

5.1. Mass conservation

Mass transfer between the liquid film and vapor core can be represented by the following mass conservation equations,

$$\frac{d\dot{m}_{Ff}}{dz} = -\Gamma_{fg} + \Gamma_d, \tag{8}$$

$$\frac{d\dot{m}_{Ef}}{dz} = -\Gamma_d, \tag{9}$$

and

$$\frac{d\dot{m}_g}{dz} = \Gamma_{fg}, \tag{10}$$

which are included in Section I of Table 3. Γ_{fg} and Γ_d can be evaluated by using energy conservation and deposition relations listed in Table 3. The deposition relation incorporates a mass transfer coefficient, k, which

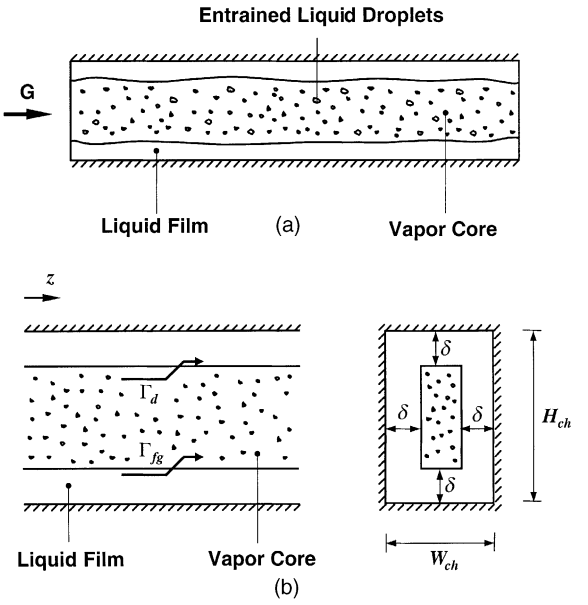

Fig. 11. (a) Schematic of annular flow pattern in micro-channel heat sink, and (b) idealized annular flow region.

is evaluated using a correlation proposed by the authors specifically for micro-channel heat sinks [11],

$$\frac{k}{j_g} = 47.8Bo\left(\frac{C}{\rho_g}\right)^{-0.147}. \tag{11}$$

Once Γ_{fg} and Γ_d are determined, local values of $\dot{m}_{Ff}$, $\dot{m}_{Ef}$, and $\dot{m}_g$ can be obtained by integrating Eqs. (8)–(10) along the stream-wise direction. Appropriate boundary conditions are required for this integration, which involve location of the onset of annular flow and the initial mass flow rate of each portion at that location. The location of the onset of annular flow is determined from a criterion for transition to annular flow by Taitel and Duckler [16,23]. According to the criterion, the Martinelli parameter has a constant value at the transition point.

$$X_{vv0} = 1.6. \tag{12}$$

The initial liquid droplet mass flow rate $\dot{m}_{Ef0}$ is given by the following correlation.

$$\frac{\dot{m}_{Ef0}}{\dot{m}} = 0.951 - 0.15\sqrt{We_{f0}}, \tag{13}$$

where We_{f0} is the Weber number of water given by

$$We_f = \frac{v_f G^2 d_h}{\sigma}. \tag{14}$$

5.2. Momentum conservation in liquid film

Momentum conservation is applied to the liquid film using the control volume shown in Fig. 12(a). The

Table 3
Key equations in annular two-phase flow model

	Equation
I	$\frac{d\dot{m}_{Ff}}{dz} = -\Gamma_{fg} + \Gamma_d; \quad \frac{d\dot{m}_{Ef}}{dz} = -\Gamma_d; \quad \frac{d\dot{m}_g}{dz} = \Gamma_{fg}$
	$\Gamma_{fg} = \frac{q''_{eff} W}{N h_{fg}}; \quad \Gamma_d = DP_c$
	$D = kC_{Ef}; \quad P_c = 2[(W_{ch} - 2\delta) + (H_{ch} - 2\delta)]$
	$C_{Ef} = \frac{\dot{m}_{Ef}}{\dot{m}_g v_g + \dot{m}_{Ef} v_f}; \quad \frac{k}{j_g} = 47.8 Bo \left(\frac{C_{Ef}}{\rho_g}\right)^{-0.147}; \quad Bo = \frac{q''_{eff} W}{N(W_{ch} + 2H_{ch}) G h_{fg}}; \quad j_g = \frac{\dot{m}_g}{\rho_g A_{ch}}$
II	$\left(-\frac{dp}{dz}\right) = \frac{3\mu_f}{P_{ch}\rho_f \delta^3}\dot{m}_{Ff} - \frac{3}{2\delta}\tau_i + \frac{3}{2\delta P_{ch}}(\Gamma_{fg} u_i - \Gamma_d u_c)$
	$u_i = \frac{2\dot{m}_{Ff}}{\rho_f (A_{ch} - A_c)}; \quad u_c = \frac{\dot{m}_{Ef} + \dot{m}_g}{\rho_c A_c}; \quad A_c = (W_{ch} - 2\delta)(H_{ch} - 2\delta); \quad \rho_c = \frac{\dot{m}_g + \dot{m}_{Ef}}{\dot{m}_g v_g + \dot{m}_{Ef} v_f}$
III	$\tau_i = \frac{1}{P_c}\left[A_c\left(-\frac{dP}{dz}\right) - P\frac{dA_c}{dz}\right] - \frac{1}{P_c}\frac{d}{dz}(\rho_c u_c^2 A_c) + \frac{1}{P_c}(\Gamma_{fg} u_i - \Gamma_d u_c)$
IV	$\tau_i = f_i\left[\frac{1}{2}\rho_c (u_c - u_i)^2\right] - \frac{\Gamma_{fg}}{2P_c}(u_c - u_i)$
	$f_i Re_c = 24(1 - 1.355\beta_c + 1.947\beta_c^2 - 1.701\beta_c^3 + 0.956\beta_c^4 - 0.254\beta_c^5)$
	$Re_c = \frac{\rho_c (u_c - u_i) d_{h,c}}{\mu_g}; \quad \beta_c = \frac{W_{ch} - 2\delta}{H_{ch} - 2\delta}; \quad d_{h,c} = \frac{4A_c}{P_c}$

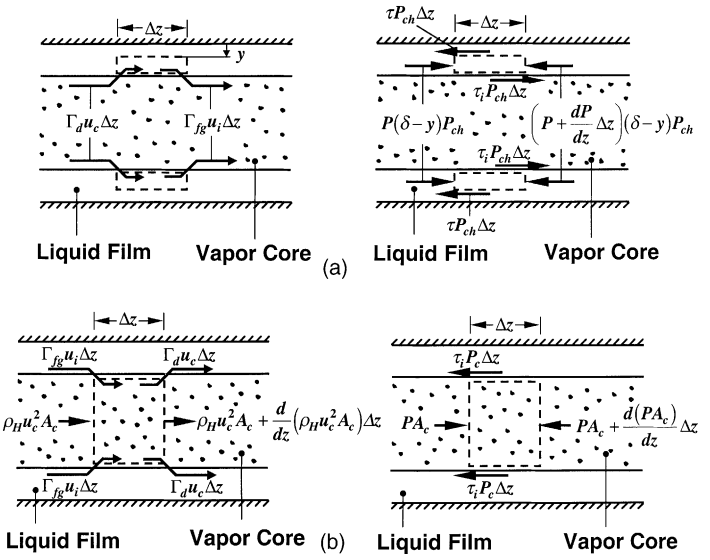

Fig. 12. Momentum conservation for control volumes encompassing (a) liquid film and (b) vapor core.

schematic to the left of Fig. 12(a) illustrates momentum exchange along the liquid film interface, and to the right the forces acting on the same control volume in the stream-wise direction. Momentum conservation yields

$$\tau = (\delta - y)\left(-\frac{dp}{dz}\right) + \tau_i - \frac{1}{P_{ch}}(\Gamma_{fg} u_i - \Gamma_d u_c). \tag{15}$$

The shear stress in the laminar liquid film can be related to the local velocity gradient by

$$\tau = \mu_f \frac{du_f}{dy}. \quad (16)$$

Substituting Eq. (16) into Eq. (15) and integrating yield the velocity profile across the film,

$$u_f = \frac{1}{\mu_f}\left(\delta y - \frac{y^2}{2}\right)\left(-\frac{dp}{dz}\right) + \frac{y}{\mu_f}\tau_i - \frac{y}{\mu_f P_{ch}}(\Gamma_{fg} u_i - \Gamma_d u_c), \quad (17)$$

which can be integrated across the liquid film thickness to yield the liquid film's mass flow rate.

$$\dot{m}_{Ff} = \frac{P_{ch}\rho_f \delta^3}{3\mu_f}\left(-\frac{dp}{dz}\right) + \frac{P_{ch}\rho_f \delta^2}{2\mu_f}\tau_i - \frac{\rho_f \delta^2}{2\mu_f}(\Gamma_{fg} u_i - \Gamma_d u_c). \quad (18)$$

Rearranging Eq. (18) yields the equation given in Section II of Table 3.

5.3. Momentum conservation in vapor core

Fig. 12(b) shows a control volume encompassing the vapor core, which is assumed a homogeneous mixture of vapor and entrained droplets. The schematic to the left illustrates momentum exchange along the interface, and to the right the forces acting on the control volume in the stream-wise direction. Equating the net momentum in the stream-wise direction to the net force leads to the equation given in Section III of Table 3.

5.4. Interfacial shear stress

The equation for interfacial shear stress between the core and liquid film is given in Section IV of Table 3. The second term on the right-hand side of this equation represents the effect of interfacial evaporation on shear stress [24]. Laminar flow is assumed in both the liquid film and vapor core.

The equations provided in Table 3 are solved simultaneously to determine the four key primary parameters of the annular flow model, $\dot{m}_{Ff}$, δ, $-(dP/dz)$, and τ_i. ΔP_{tp} is then evaluated by integrating $-(dP/dz)$ along the micro-channel.

Fig. 13(a) and (b) compare ΔP_{pred} using the annular flow model to ΔP_{exp} for representative conditions and for the entire database from the present study, respectively. Both figures show excellent predictive capability, with a MAE of 12.7%, virtually matching the accuracy of the best of all the correlations tested.

Aside from its excellent predictive capability, the annular flow model possesses the unique attributes of providing a detailed description of the various transport processes occurring in two-phase micro-channel heat sinks, as well as fundamental appeal and broader application range than correlations.

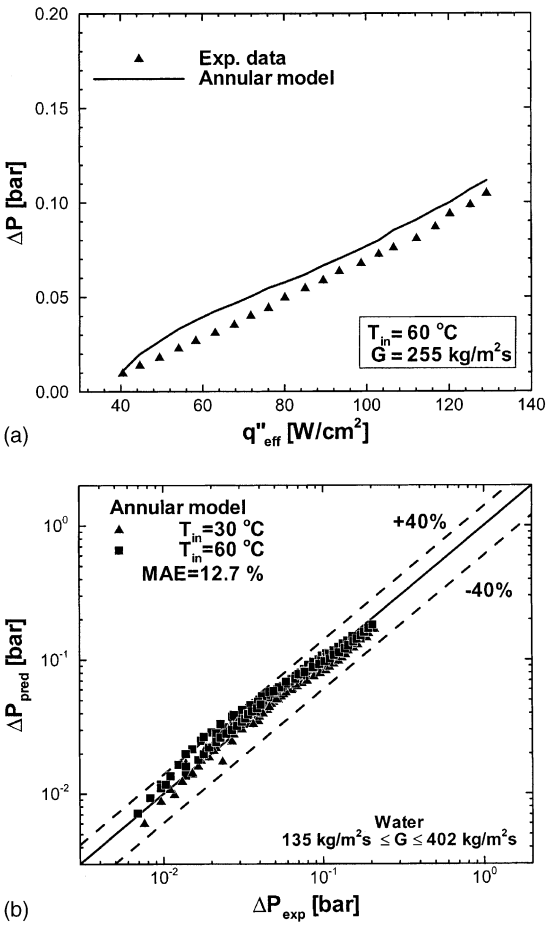

Fig. 13. Comparison of annular two-phase flow model predictions with pressure drop data for (a) $T_{in} = 60$ °C and $G = 255$ kg/m^{2}s, and (b) entire database.

6. Conclusions

In this study, experiments were performed to measure pressure drop in a two-phase micro-channel heat sink. Two different predictive approaches were examined for suitability to micro-channel pressure-drop prediction, empirical correlations and a new theoretical annular flow model. Key findings from the study are as follows:

(1) Two types of two-phase instability were encountered: pressure drop oscillation and parallel channel instability. Pressure drop oscillation produces fairly periodic, large-amplitude flow oscillations, which are the result of interaction between vapor generation

in channels and compressible volume in the flow loop upstream of the heat sink. Parallel channel instability, on the other hand, produces only mild flow fluctuations, which are the result of density wave oscillation within each channel and feedback interaction between channels. The severe pressure drop oscillation, which can trigger pre-mature CHF, can be eliminated simply by throttling the flow upstream of the heat sink.

(2) Pressure drop increases appreciably upon commencement of boiling in micro-channels. At both moderate and high heat fluxes, the flow oscillates between the slug and annular patterns upstream and is predominantly annular downstream.

(3) Six widely used models and macro-channel correlations were examined in predicting pressure drop in the two-phase region. Correlations based on turbulent flow overpredict the data by large margins, while those incorporating the combination of laminar liquid and laminar vapor flow yield better agreement with the data.

(4) Better accuracy is achieved using correlations specifically developed for mini/micro-channels. A new correlation is proposed which incorporates the effects of both channel size and coolant mass velocity to improve pressure drop prediction.

(5) An annular flow model is proposed as an alternative method to predicting two-phase pressure drop. Its accuracy matches that of the best of all the correlations tested. This model is recommended for heat sink design because of its ability to provide a detailed description of the various transport processes occurring in the micro-channel.

Acknowledgements

The authors are grateful for the support of the Office of Basic Energy Sciences of the US Department of Energy (Award no. DE-FG02-93ER14394 A7).

References

[1] M.B. Bowers, I. Mudawar, High flux boiling in low flow rate, low pressure drop mini-channel and micro-channel heat sinks, Int. J. Heat Mass Transfer 37 (1994) 321–332.

[2] M.B. Bowers, I. Mudawar, Two-phase electronic cooling using mini-channel and micro-channel heat sinks: Part 1—design criteria and heat diffusion constraints, J. Electron. Packaging 116 (1994) 290–297.

[3] M.B. Bowers, I. Mudawar, Two-phase electronic cooling using mini-channel and micro-channel heat sinks: Part 2—flow rate and pressure drop constraints, J. Electron. Packaging 116 (1994) 298–305.

[4] T.N. Tran, M.C. Chyu, M.W. Wambsganss, D.M. France, Two-phase pressure drop of refrigerants during flow boiling in small channels: an experimental investigation and correlation development, Int. J. Multiphase Flow 26 (2000) 1739–1754.

[5] S.M. Zivi, Estimation of steady-state steam void-fraction by means of the principle of minimum entropy production, J. Heat Transfer 86 (1964) 247–252.

[6] H.J. Lee, S.Y. Lee, Heat transfer correlation for boiling flows in small rectangular horizontal channels with low aspect ratios, Int. J. Multiphase Flow 27 (2001) 2043–2062.

[7] H.J. Lee, S.Y. Lee, Pressure drop correlations for two-phase flow within horizontal rectangular channels with small heights, Int. J. Multiphase Flow 27 (2001) 783–796.

[8] W. Yu, D.M. France, M.W. Wambsganss, J.R. Hull, Two-phase pressure drop, boiling heat transfer, and critical heat flux to water in a small-diameter horizontal tube, Int. J. Multiphase Flow 28 (2002) 927–941.

[9] S.G. Kandlikar, M.E. Steinke, S. Tian, L.A. Campbell, High-speed photographic observation of flow boiling of water in parallel mini-channels, in: Proceedings of 35th National Heat Transfer Conference, ASME, Anaheim, CA, 2001, pp. 675–684.

[10] G. Hetsroni, A. Mosyak, Z. Segal, G. Ziskind, A uniform temperature heat sink for cooling of electronic devices, Int. J. Heat Mass Transfer 45 (2002) 3275–3286.

[11] W. Qu, I. Mudawar, Flow boiling heat transfer in two-phase micro-channel heat sinks—II. Annular two-phase flow model, International Journal of Heat and Mass Transfer, (2003), doi:10.1016/S0017-9310(03)00042-5.

[12] A.E. Bergles, Review of instability in two-phase systems, in: S. Kakac, F. Mayinger (Eds.), Two-Phase Flows and Heat Transfer, vol. 1, Hemisphere, Washington, 1977, pp. 383–422.

[13] G. Yadigaroglu, Two-phase flow instabilities and propagation phenomena, in: J.M. Delhaye, et al. (Eds.), Thermohydraulics of two-phase systems for industrial design and nuclear engineering, Hemisphere, Washington, 1981, pp. 353–403.

[14] R.K. Shah, A.L. London, Laminar Flow Forced Convection in Ducts: A Source Book for Compact Heat Exchanger Analytical Data, Supl. 1, Academic press, New York, 1978.

[15] R.D. Blevins, Applied Fluid Dynamics Handbook, Van Nostrand Reinhold Company, New York, 1984.

[16] J.G. Collier, J.R. Thome, Convective Boiling and Condensation, Third ed., Oxford University Press, Oxford, 1994.

[17] R.W. Lockhart, R.C. Martinelli, Proposed correlation of data for isothermal two-phase, two-component flow in pipes, Chem. Eng. Prog. 45 (1949) 39–48.

[18] D. Chisholm, Two-Phase Flow in Pipelines and Heat Exchangers, Longman, New York, 1983.

[19] R.C. Martinelli, D.B. Nelson, Prediction of pressure drop during forced-circulation boiling of water, Trans. ASME 70 (1948) 695–702.

[20] D. Chisholm, Pressure gradients due to friction during the flow of evaporation two-phase mixtures in smooth tubes and channels, Int. J. Heat Mass Transfer 16 (1973) 347–358.
[21] K. Mishima, T. Hibiki, Some characteristics of air–water two-phase flow in small diameter vertical tubes, Int. J. Multiphase Flow 22 (1996) 703–712.
[22] S. Mukherjee, I. Mudawar, Pumpless loop for narrow channel and micro-channel boiling, J. Electron. Packaging, in press.
[23] Y. Taitel, A.E. Dukler, A model for predicting flow regime transitions in horizontal and near horizontal gas–liquid flow, AIChE J. 22 (1976) 47–55.
[24] G.B. Wallis, One Dimensional Two-Phase Flow, McGraw-Hill, New York, 1969.